

FY21 Los Alamos National Laboratory Experimental Campaigns at the Omega Laser Facility

Mshock 2021: Effects of Heating on Instability Growth

Principal Investigators: K. A. Flippo, F. W. Doss, A. Rasmus, C. Di Stefano, B. Tobias, and E. C. Merritt

The LANL High-Energy-Density Hydro team has adapted our OMEGA Shear instability platform to study the effects of heating on a mixing interface similar to what might occur in the inner shell of a double-shell-type inertial confinement fusion (ICF) design. The platform is motivated by simulations presented in Haines *et al.*¹ that suggested the timing of heating can have a significant impact on instability development. These experiments are an extension of previous work in 2020, where we had adapted a similar Richtmyer–Meshkov (RM)/Rayleigh–Taylor (RT) platform for studying the effects of heating on instability growth under shock–reshock conditions. In both platforms the mixing interface can be heated before, after, or during shock arrival and instability onset using hot-electron and x-ray emission from driven CH foils surrounding the main target at a distance. The current design allows for heating of a high-density interface surrounded by low-density foam. The mixing layer material can be chosen with any density and/or composition, but we typically chose solid-density plastic or metal foils, which can be heated from several eV up to around 100 eV depending on layer material and thickness and heater drive laser power. Strong shocks (from the drive beams) can then interact with these layers from either end of the shock tube. These experiments are intended as platform development for heated instability platform for OMEGA and as proof of principle for adaption to larger facilities such as the National Ignition Facility (NIF) as well.

In this experiment we use several variations of the LANL Shear Platform to test the effects of heat deposition on the mixing layer (heat flux out of the layer) and across the mixing layer (heat flux into the layer), but changing the materials (absorption properties) of various target components. The shear target (Fig. 1) is composed of a Be shock tube containing two hemi-cylindrical foams separated by a solid-density foil. At either end of the tube is a gold plug that blocks the shock on that side of the foil, creating a system of two counter-propagating shocks on either side of a mixing layer. In these experiments the tracer foil and foam are either Fe (high absorption) and 100 mg/cm³ CH (low absorption) to test heat flux out of the layer, or Be (low absorption) and 100 mg/cm³ Cu-doped CH (high absorption) to test heat flux into the layer. The shock tube is surrounded by several 10- μ m-thick CH foils driven by eight to nine beams that offer about 4 kJ of laser energy of which about 50% to 25% can be converted into hot electrons and x rays for heating the target. The main target also has an attached ten-inch manipulator TIM-6 backlighter (BL) that can be used to test a Fresnel zone plate array, and the setup has a TIM-2–inserted BL for use with the primary x-ray framing camera (XRFC) on TIM-3.

Experiments showed we were able to heat the target with no significant heating asymmetry as observed in the RM/RT platform (Fig. 2). This is consistent with our expectation that the Shear Platform would show more-uniform heating due to the mixing plane being orthogonal to the heating sources. We do see significant new structure in the radiographs of the heated mixing layer for both target material variations. However, the images also show more background shock structure, indicating that we may be driving radially inward shocks from heating the tube. Future experiments will help us determine how much of the new structure in the mixing layer is an effect of extra transient shocks, and how much is due to heating; they will also help us develop potential mitigation strategies for tube heating.

This work was supported by Los Alamos National Laboratory under Contract No. 89233218CNA000001 with Triad National Security, LLC.

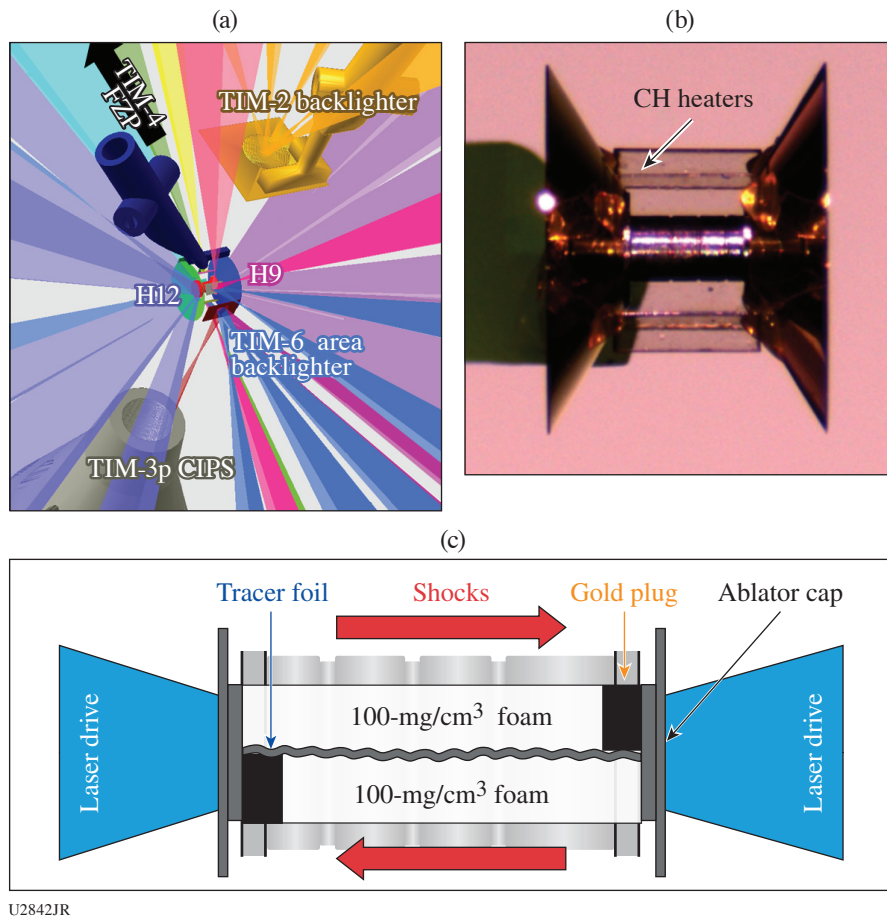


Figure 1

(a) VisRad model of the shock-tube target, associated shock drive and heater drive beams, BL target, and diagnostic lines of sight. (b) Pre-shot target photograph with CH heater foils. (c) Schematic of the Shear physics package.

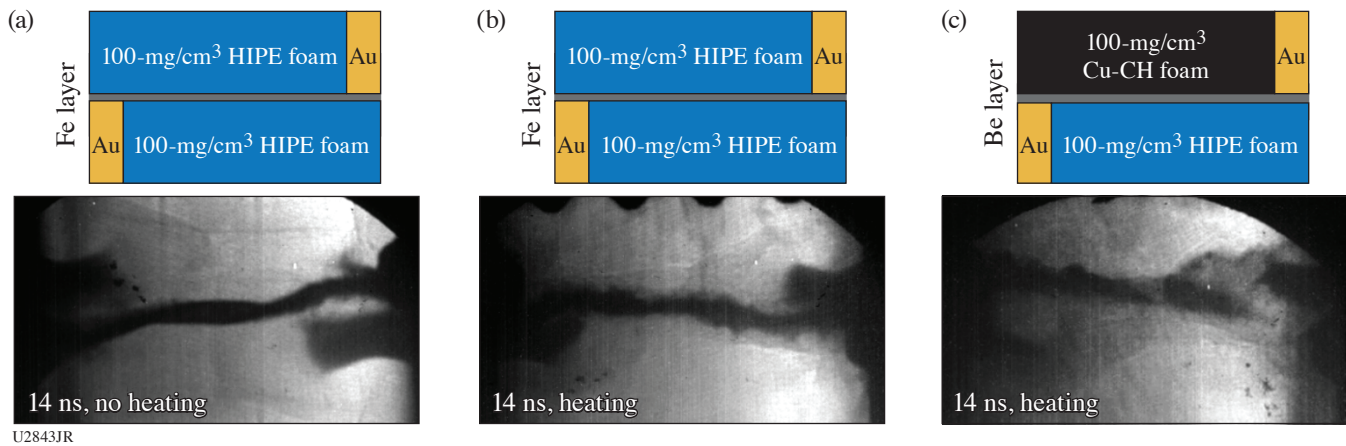


Figure 2

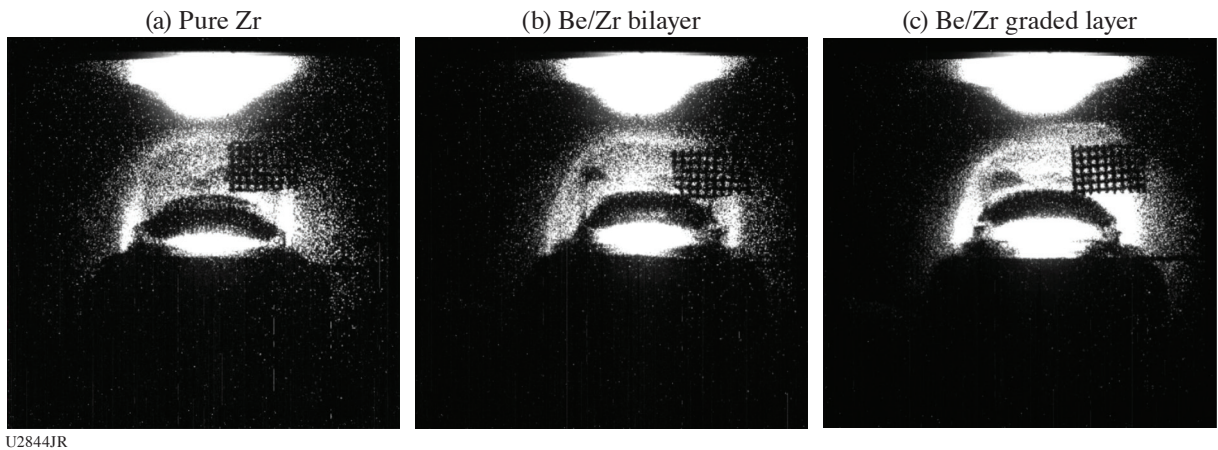
Radiography data of two target types with and without heating, at late times in the shear layer development.

DSPlanar

Principal Investigators: A. Rasmus, S. Palaniyappan, E. Loomis, D. Stark, N. Christensen, and A. Strickland

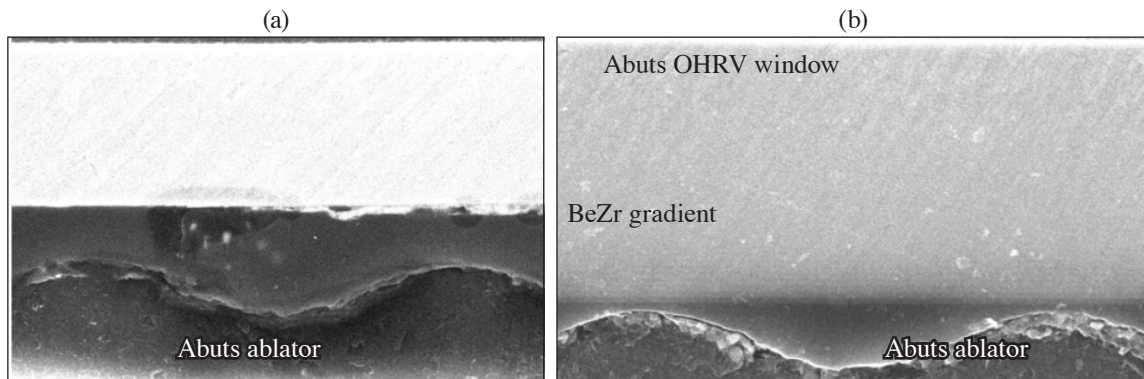
The Double-Shell Campaign uses a two-shell ICF target. Between the outer and inner shells, a foam cushion is used to assist in the transfer of momentum between the two shells. The inner shell is typically a high-Z metal. The large-density jump between the foam and inner shell presents an interface that is highly unstable to fluid instabilities due to the large Atwood number. A lower-density “tamper” (e.g., beryllium) is typically used to step the density transition between inner shell and foam pusher. A density gradient can be used to further damp instability growth. DSPlanar-21A and B aimed to test the damping of instability growth by a density gradient by measuring the impact of a density gradient on interface perturbation growth using radiography (21A) and on shock ripples using the OMEGA high-resolution velocimeter (OHRV), 2-D VISAR (velocity interferometer system for any reflector) diagnostic (21B).

DSPlanar-21A used radiography to compare hydrodynamic instability growth in pure-Zr layers, Be/Zr bilayers, and Be/Zr graded layers (see Figs. 3 and 4). The measured instability growth shows reduced growth in both the bilayer and graded-layer targets compared to the pure-Zr layer; however, among the bilayer and the graded layer, the difference in growth is not significant.



U2844JR

Figure 3
Radiographs of hydrodynamic instability growth in a (a) pure-Zr layer, (b) Be/Zr bilayer, and (c) Be/Zr graded layer.



U2845JR

Figure 4
SEM images of (a) a Be/Zr bilayer and (b) a graded layer. A sinusoidal perturbation is machined onto the Be face of each layer to seed a shock ripple.

DSPlanar-21B attempted to measure a difference between instability growth in the graded and bilayers by using the OHRV diagnostic and measuring a different aspect of instability growth, i.e., shock ripples instead of interface perturbations. DSPlanar-21B targets consisted of a stacked set of materials designed to produce a shock, imprint a ripple on it, damp the ripple by propagating it through a graded or steep material transition, and finally image the rippled shock inside a PMMA window (see Fig. 5). Be/Zr graded layers and bilayers (see Fig. 4), as well as Be/W graded layers, were shot. DSPlanar-21B achieved a limited set of physics goals due to the unavailability of the OHRV. As such, we shot our joint active shock breakout (ASBO)/OHRV targets using only the ASBO diagnostic. This reduced data set allowed us to troubleshoot blanking issues with our target stack and gain insight into shock timings and strengths in our targets.

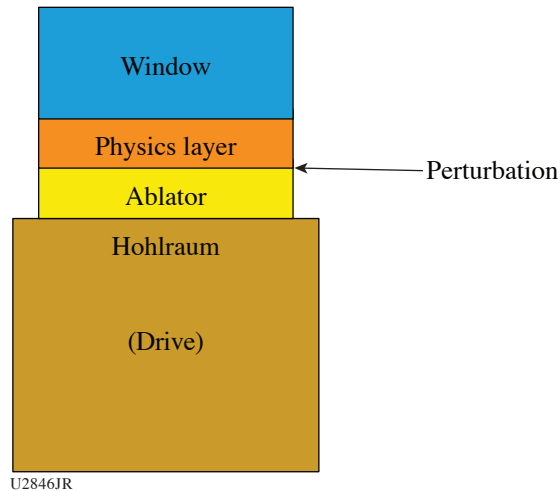


Figure 5
A schematic of DSPlanar-21B targets.

Gas-Filled Cylindrical Implosion at the Omega Laser Facility

Principal Investigators: S. Palaniyappan, J. P. Sauppe, L. Kot, K. A. Flippo, A. Strickland, T. Day, R. Roycroft, K. L. Stalsberg, and J. L. Kline

The CylDRT21A shot day was designed to study the nonlinear growth of the deceleration-phase RT growth in gas-filled and foam-filled scale-1 cylindrical implosion. The aluminum marker in the scale-1 cylinder has the nominal $m = 20$ sine wave perturbation with $4\text{-}\mu\text{m}$ amplitude on the inner side of the marker layer. We had two main goals for this shot day: (1) to study hydro-scaling between a NIF scale-3 cylinder implosion and an OMEGA scale-1 implosion with low foam-fill density at a convergence ratio of ~ 5 ; and (2) to test a propane gas-filled (10 mg/cm^3 , i.e., $\sim 5\text{-atm}$ pressure) scale-1 cylinder implosion in preparation for the FY22 NIF gas-filled cylindrical implosion.

Figure 6 shows the VisRad model of the foam-filled cylindrical implosion experiment. The main cylinder target is inserted via TIM-5 (also used as the gas fill line) and aligned along the P6–P7 axis. The TIM-4 axial backlighter (Fe) is attached to the main cylinder target. We use x-ray framing camera 3 (XRFC3) in TIM-6 to capture the on-axis radiograph of the cylinder and will use a nose tip with $12\times$ magnification with a $10\text{-}\mu\text{m}$ pinhole for the axial radiography. We also have $20\text{-}\mu\text{m}$ pinholes for backup. For the side view along the TIM-2/TIM-3 axis, we use $6\times$ magnification, a $15\text{-}\mu\text{m}$ single pinhole, and XRFC4 with a single strip. The sidelighter (V) is inserted via TIM-2.

Figure 7 shows the synthetic x-ray radiograph of the 10-mg/cm^3 gas-filled cylindrical implosion from the *xRAGE* simulation. The corresponding experimental figure is shown in Fig. 8 along with the side-on radiograph. The measured radiograph differs from the pre-shot calculation in the radial extent of the aluminum marker on the outer side. We are performing post-shot simulations to better understand the measured growth in comparison to the pre-shot simulation.

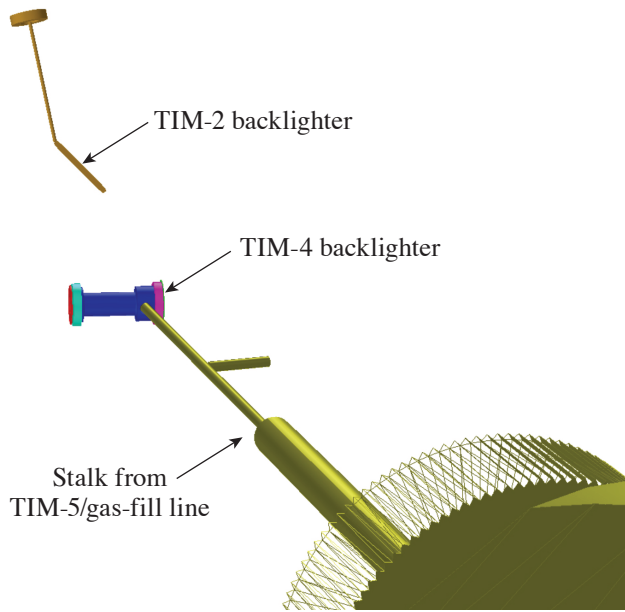
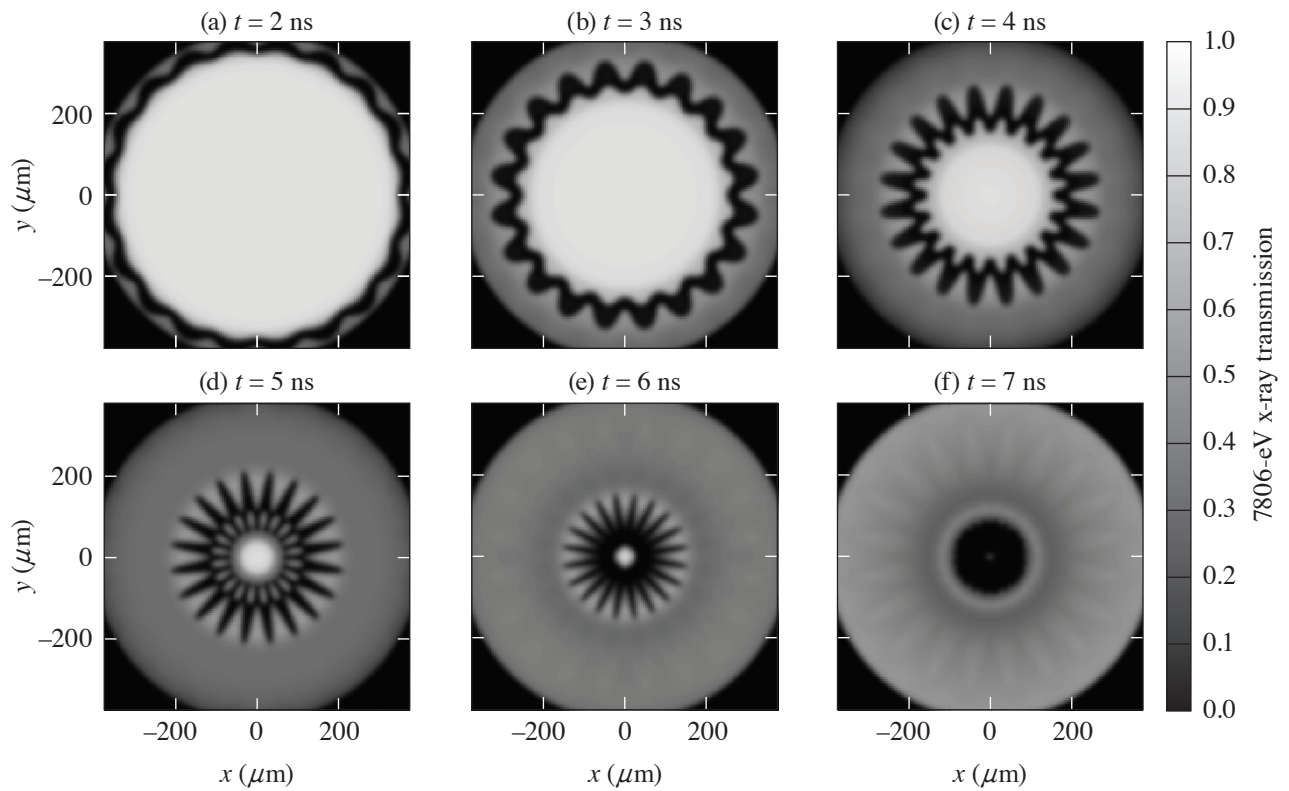


Figure 6
Experimental setup on OMEGA EP for proton beam generation.

U2847JR



U2848JR

Figure 7
Synthetic radiograph of the 10-mg/cm³ gas-filled cylindrical implosion with mode-20 sine wave initial perturbation from *xRAGE* calculation.

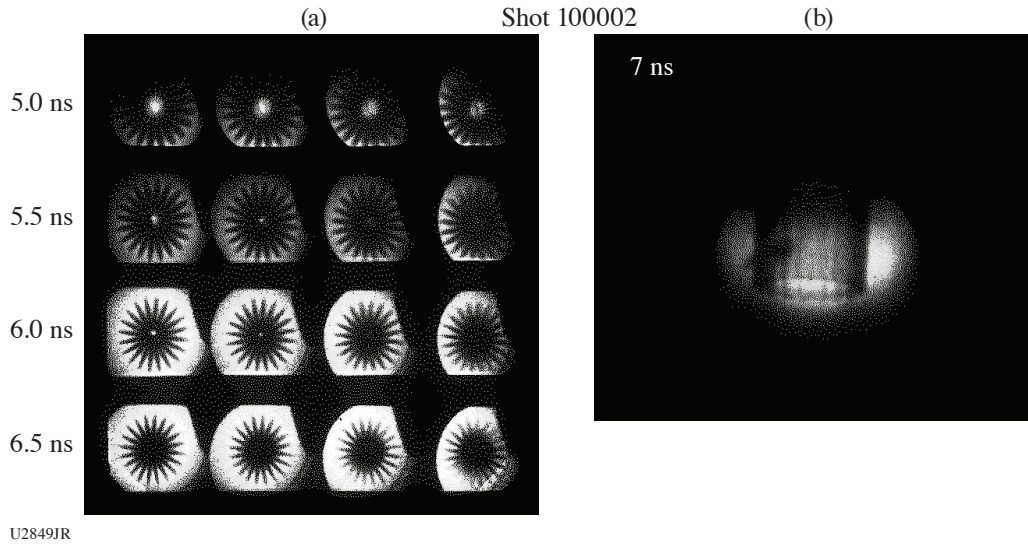


Figure 8
Experimental radiograph of the 10-mg/cm³ gas-filled cylindrical implosion. (a) Axial radiograph and (b) side-on radiograph.

Laser-Driven Proton Radiography of Shocked Plastic Foil

Principal Investigators: S. Palaniyappan, C. Huang, A. Favalli, D. Broughton, and R. Reinovsky (LANL); and S. Klein (University of Michigan)

1. Multi-Probe 21A

The goal for the FY21 Multi-Probe Project was to generate short-pulse laser-driven protons and radiograph the shocked plastic foil with those protons. During the Multi-Probe 21A shot day we characterized the protons generated from a short-pulse-driven thin plastic foil. Later, during the Multi-Probe 21B shot day, we used those protons to image a shocked plastic foil.

We generated a proton beam on OMEGA EP by driving a thin plastic foil with the sidelighter beam. The sidelighter beam delivered a maximum of 500 J with a 0.7-ps pulse duration. The foil thickness was 600 nm. The protons were detected using a radiochromic film (RCF) film pack held by the near-target arm (NTA) (see Fig. 9). Some plastic targets had a CPC (compound parabolic concentrator) in front of them to help better focus the laser beam.

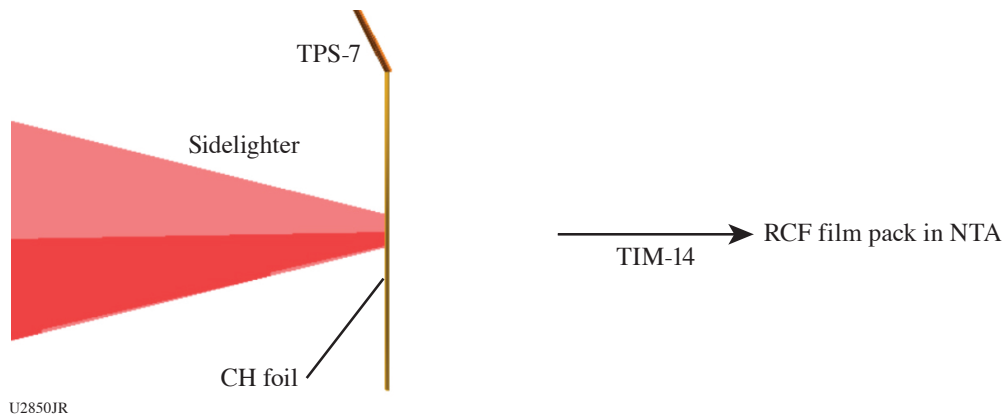
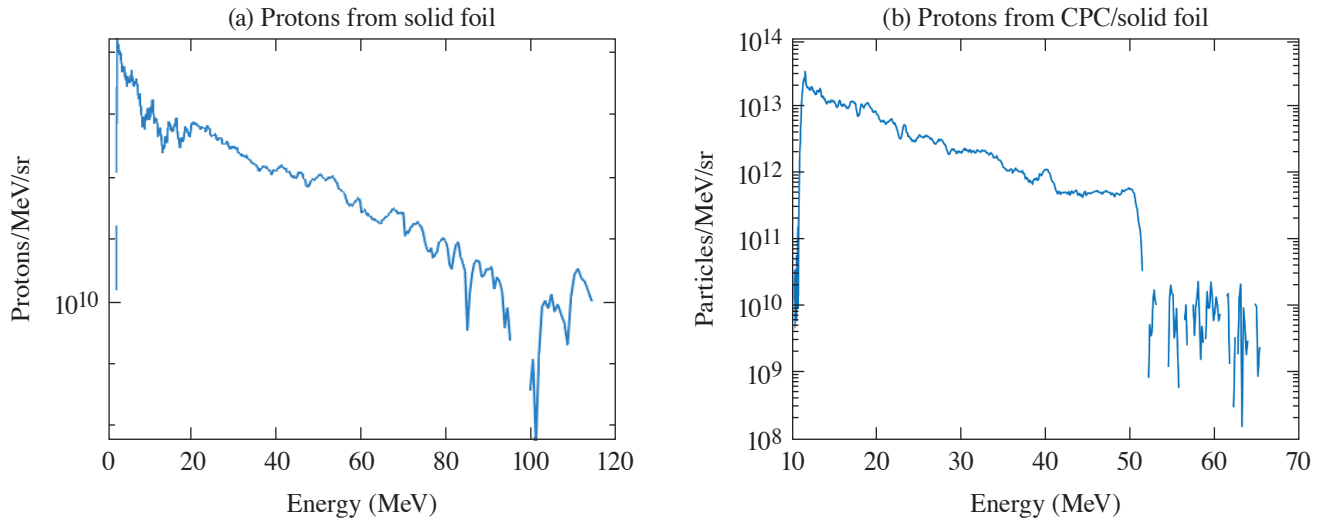


Figure 9
Experimental setup on OMEGA EP for proton-beam generation. TPS: Target Positioning System.

Figure 10 shows the measured proton spectra from both the thin plastic foil and the same foil with a CPC cone in the front. Compared to the targets with the CPC cones, the foils alone performed much better and generated protons up to ~100 MeV in energy. In comparison, the targets with the CPC cone generated protons up to 50 MeV in energy. This is contrary to what we had expected originally. Therefore, we decided to use only the thin plastic foils without the CPC cone for our future proton-generation experiments.

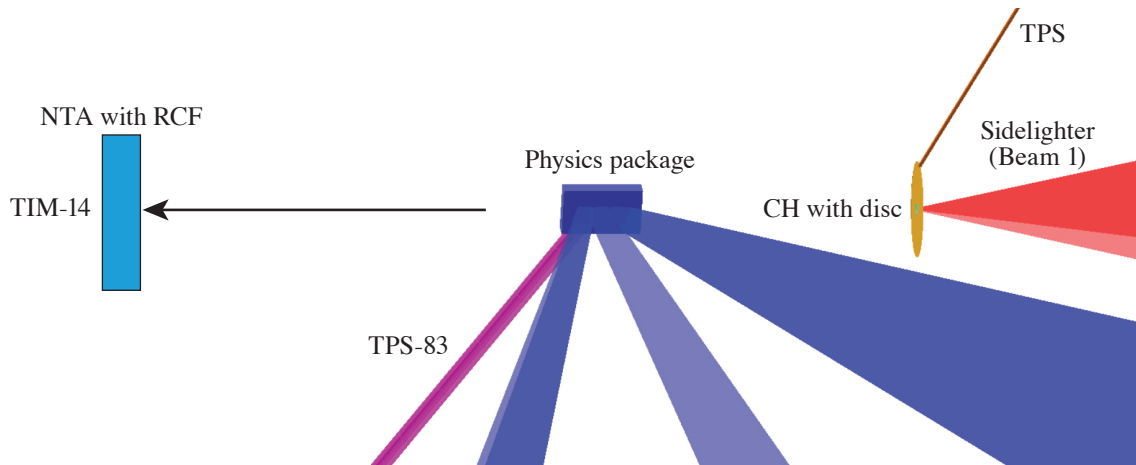


U2851JR

Figure 10
Measured proton spectra from (a) thin plastic foil and (b) thin plastic foil with CPC in the front.

2. Multi-Probe 21B

Figure 11 shows the experimental setup on OMEGA EP for proton radiography. The proton beams are generated from a short-pulse-driven thin plastic foil. Three long-pulse UV beams arranged in a line drive the physics package. The protons are detected using an RCF pack in TIM-14 held by the NTA.



U2852JR

Figure 11
Experimental setup on OMEGA EP for proton radiography.

Figure 12 shows the proton radiograph of the shock-driven thin plastic foil. We are currently working on understanding the proton radiograph.

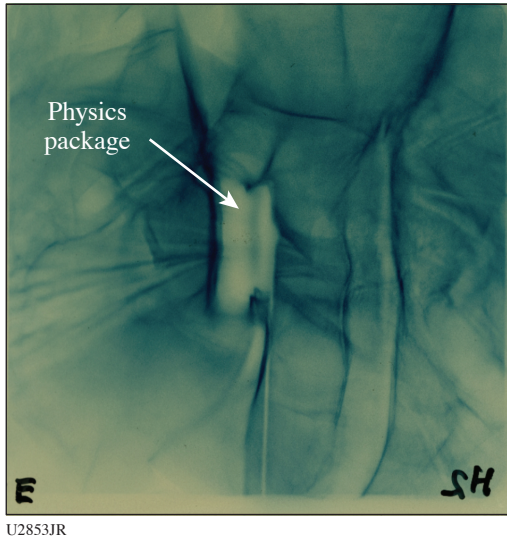


Figure 12
Proton radiograph of a shocked thin plastic foil.

Evaluation of Two-Photon Polymerization Printed Structures as Low-Density Supports in Multishell Targets

Principal Investigators: B. S. Scheiner, M. J. Schmitt, D. W. Schmidt, and L. Goodwin (LANL); and F. J. Marshall, P. M. Nilson, and R. S. Craxton (LLE)

The *Revolver 20 B/C* (delayed to FY21) Campaigns evaluated the fabrication and use of low-density (5- to 20-mg/cm³), two-photon polymerization (2PP) printed structures as a support for the inner shell of a direct-drive double-shell target.² The 2PP hemispherical structures, an example of which is shown in Fig. 13(a), were printed in a stochastic Voronoi lattice geometry³ and were composed of CH_{1.72}N_{0.086}O_{0.37}. From 1-D and 2-D simulations, it is expected that the lattices will begin to disassemble by absorbing the radiation from the ablator’s hot corona that penetrates the ablator shell. The extent to which

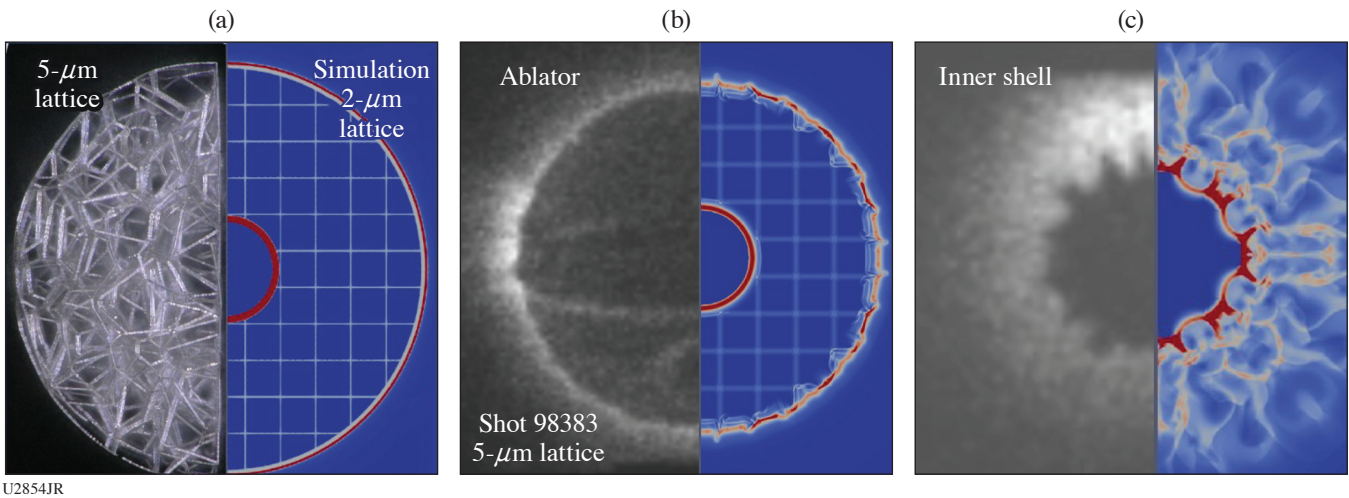


Figure 13
(a) An image of the 2PP inner-shell support is compared to the initial lattice of the cylindrical simulations. (b) Perturbations on the ablator surface due to the lattice are observed in both experiments and simulations. (c) Simulations are able to predict significant perturbations on the outer surface of the inner shell when the 2PP lattice disassembly is insufficient.

it can do so before bulk motion of the ablator depends on the lattice strut size and potentially on the lattice's ability to absorb x-ray radiation. In experiments, the extent of the lattice disassembly is determined by measuring the perturbations imparted to the ablator, measured by self-emission radiography as shown in Fig. 13(b), and to the inner metal shell, measured via 6.7-keV backlit radiography⁴ as shown in Fig. 13(c). Cylindrical simulations of surrogate lattice structures in the r - θ plane qualitatively exhibit many of the features shown in the radiographs. On the ablator, the pressure of the lattice struts against the imploding ablator shell results in bumps on the ablator surface seen in Fig. 13(b). On the inner shell, a nonuniform shock formed by the interaction of the perturbed, preheated metal shell with the residual lattice results in significant growth of spatial nonuniformity. This is seen qualitatively in the simulations and inner-shell radiograph of Fig. 13(c). Follow-on experiments at near full scale on the NIF, where implosion time scales will be greater by a factor of 5, will assess the perturbation reduction owing to more-complete lattice disassembly.

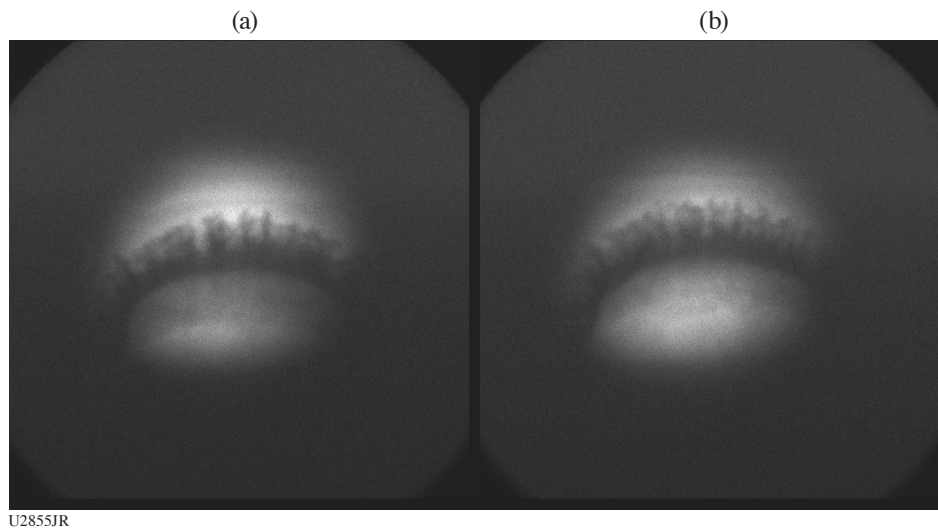
This research was supported by the Laboratory Directed Research and Development Program of Los Alamos National Laboratory under Project Number 20180051DR.

FY21 ModCons Experiments

Principal Investigators: A. Rasmus, J. Levesque, C. Di Stefano, K. A. Flippo, E. Merritt, F. Doss, K. Love, N. Christiansen, A. Strickland, and D. Schmidt

In FY21, the ModCons EP Campaign did a combination of data collection and diagnostic development. ModCons experiments utilize a shared experimental platform to study different aspects of hydrodynamic-instability growth on interfaces. Three long-pulse beams are used to create a semi-sustained shock, which drives instability growth. These campaigns utilize a Mn He $_{\alpha}$ (6.2-keV) backlighter, which is used in conjunction with the spherical crystal imager (SCI) or Fresnel zone plate (FZP) to create x-ray radiographs of interface evolution.

ModCons 21A measured the evolution of RM, with delayed-onset RT, for a broadband perturbation. This experiment finished a data set that examined how initial conditions alter multimode instability growth. In particular, we kept the wavelengths in the perturbation the same but weighted the amplitudes so that either short or wavelength modes dominated (see Fig. 14). These data will inform the initialization of sub-grid models of turbulence.



U2855JR

Figure 14

SCI images of multimode RM+ RT growth comparing how instability growth for initial perturbations biased toward (a) long- or (b) short-wavelength modes.

ModCons EP 21B was the first ModCons shot day that adapted the ModCons EP Platform to conditions relevant to the NIF MShock Campaigns studying successive shocks on a perturbed tracer layer. The goal of this campaign is to use scaled OMEGA EP experiments to supplement the NIF data by allowing us to observe interface growth at early times during the direct-drive-only portion of the NIF experiments. These experiments use the same shock tube and foam materials as the Mn SCI x-ray imaging setup from prior ModCons experiments. Changes to the platform include an additional ablator stack of CH and Au that is present on the NIF platform; also the laser drive will use three simultaneous beams at maximum power over a 1-ns pulse to reach intensities $\sim 600 \text{ TW/cm}^2$, roughly equivalent to the direct-drive energy used on the NIF MShock experiments prior to August 2021. For the first shot day, we used two single-mode sinusoidal perturbation types that had previously been used on the NIF experiments— $275\text{-}\mu\text{m}$ wavelength at $28\text{-}\mu\text{m}$ amplitude and $150\text{-}\mu\text{m}$ wavelength at $5\text{-}\mu\text{m}$ amplitude (see Fig. 15). We imaged the systems at 20, 23, 26, and 29 ns, from which we can compare the interface position to NIF results and simulations.



Figure 15
Filtered x-ray image of a $\lambda = 275\text{-}\mu\text{m}$ wavelength, amplitude = $28\text{-}\mu\text{m}$ perturbation at 29 ns after laser drive. The shapes around the edges are a spatial fiducial.

The measured interface positions from the ModCons-21B experiments suggest the system is consistently slower than the NIF results from experiments before August 2021. The modified NIF MShock Platform from August 2021 onward uses a reduced direct-drive intensity, and the trajectory of the new platform matches the OMEGA EP trajectory well. The continuation of this series will use the perturbation profile of the more-recent NIF MShock experiments and will attempt to improve analysis of mix parameters by averaging over multiple images at the same time over different shots (see Fig. 16).

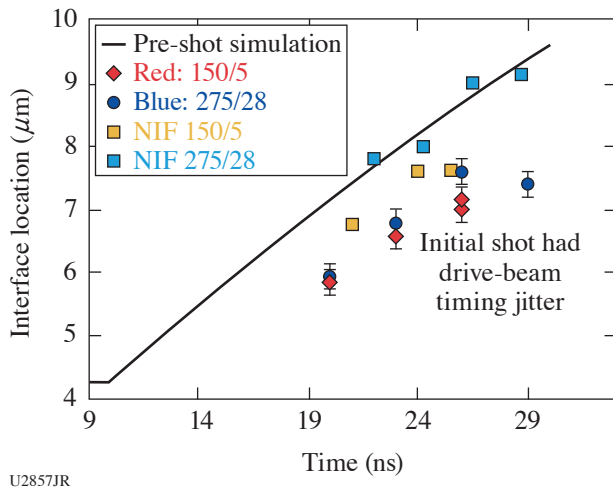


Figure 16
Comparison of the interface position over time for the OMEGA EP and NIF MShock experiments.

ModCons-21C fielded the LANL FZP diagnostic. These experiments established the survivability of the FZP's at small standoffs but did not obtain high-resolution images. We will be working on testing our FZP design on the benchtop moving forward and will then look at fielding them in experiments again once we understand how to field them better in a controlled environment.

OUTI Experimental Campaign Annual Report

Principal Investigators: H. M. Johns, P. M. Kozlowski, H. F. Robey, C. Fryer, S. Wood, T. Byvank, S. Coffing, T. S. Perry, C. J. Fontes, T. Urbatsch, and M. Douglas

The OUTI Experimental Campaign builds upon previous COAX⁵ and Radishock⁶ experimental campaigns. The stated goal of the campaign was to experimentally measure transmission (including bound-free) and temperature for transport across a density boundary that is handled differently by Sn/IMC numerical radiation transport. The goals of FY21 were to collect initial data required to develop a true-transmission analysis method in contrast to the previous bound-bound transmission-only method,⁵ to collect proof-of-concept data for collecting spectra from the outer foam in a COAX-like target, and to make improvements to the radiography side of the platform to reduce experimental uncertainties with respect to the COAX and Radishock Campaigns. OUTI21A collected 11 shots on 24 February 2021, while OUTI21B collected 7 shots on 5 August 2021 (Fig. 17).

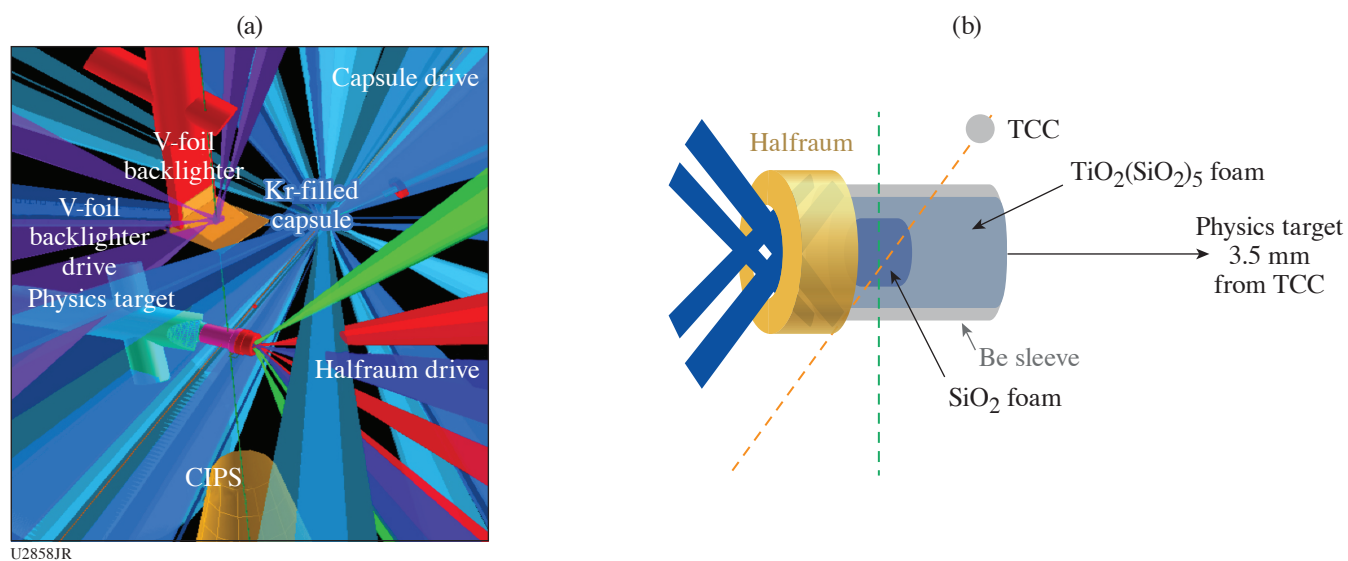
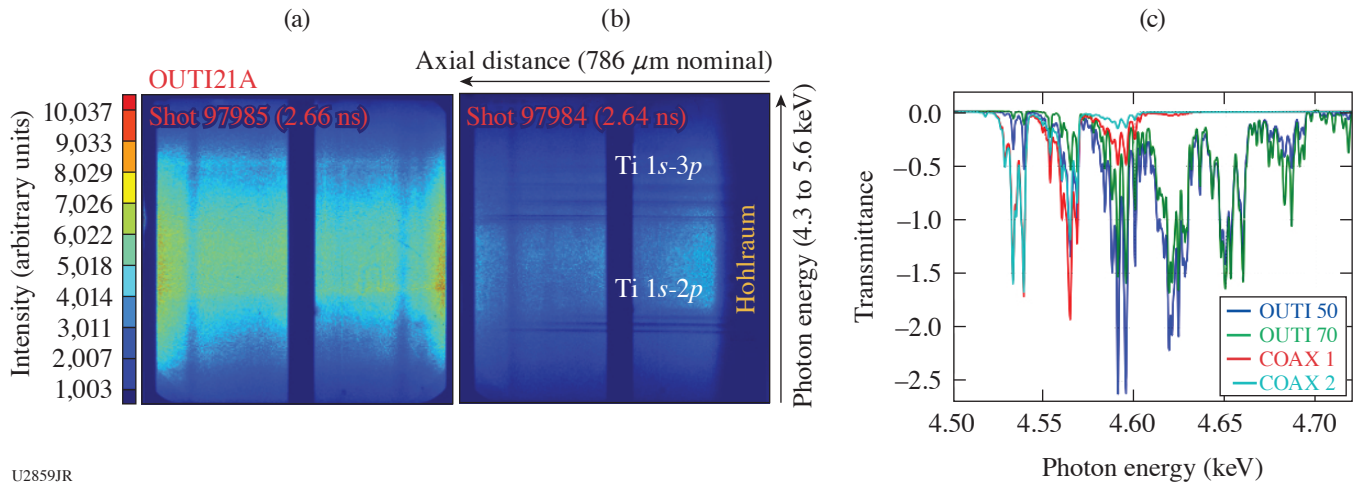


Figure 17

(a) VisRad display of the OUTI experimental campaign with close-up of OUTI physics target. (b) The OUTI physics target is a COAX-like⁵ target in reverse, with the outer foam containing Ti-laden foam and the inner foam containing only SiO₂. The platform itself draws heavily from the prior Radishock Campaign,⁶ using the same capsule and capsule drive, the same hohlraum and hohlraum drive, and the same V-foil backlighter. Due to differences in the physics target design, the final radiography design used three beams, while Radishock used five beams. TCC: target chamber center.

Prior to OUTI21A, no attempt had been made to capture absorption spectra from a region of the foam that was not driven by the halfraum. Because the size of the REH is limited to the radius of the inner foam, heat transport across the radius of the target, and therefore across any density boundary, must occur in order for absorption spectra to be obtained from dopant in the outer foam. Calculated COAX and OUTI spectra are shown in Fig. 18(c) for the same 20% TiO₂ and 80% SiO₂ molar ratio as was fielded in COAX.⁵ OUTI21A collected proof-of-concept data for this approach, also shown in Fig. 18(c). An examination of the flat-field data in comparison to continuum from the physics target shot 97984 shows that the intensity of even-continuum regions is much lower after passing through the physics target, as expected due to absorption from the SiO₂ foam and Ti bound-free absorption. In OUTI21B we intended to qualify a duplicate spectrometer to enable collection of a flat-field for every physics target shot; however, significant facility maintenance issues meant that while we were able to verify the efficacy of the new spectrometer, we were not able to collect the desired spectra and must do so on a later shot day in FY22. To verify that the new spectrometer works as intended, we collected a three-filter (Sc, Ti, V) dispersion measurement with both spectrometers.



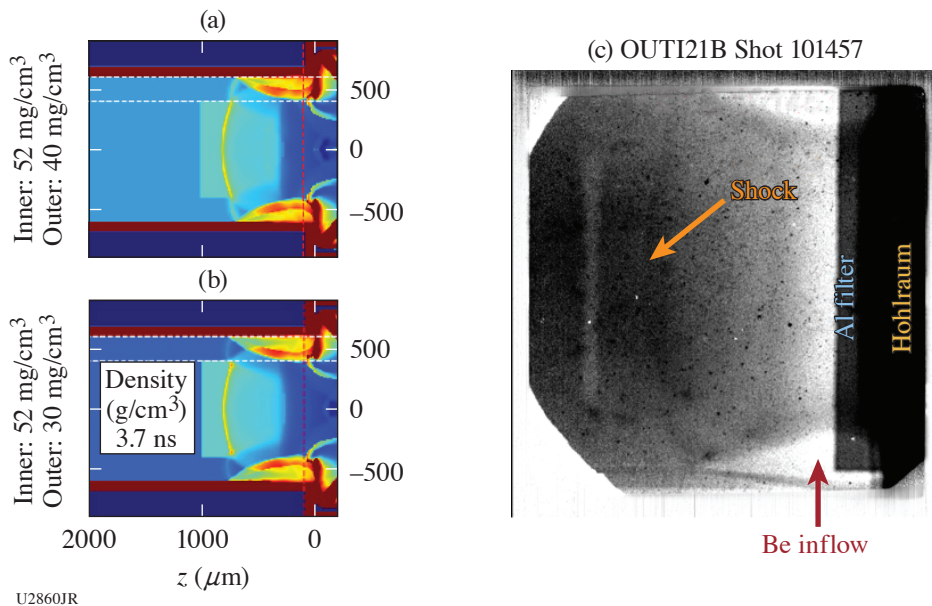
U2859JR

Figure 18

Wedge corrected data for (a) a flat-field shot 97985 and (b) a physics target shot 97984 are shown with a common intensity scale. (c) Calculated Ti K-shell spectra are shown for COAX with 50- and 70-mg/cm³ foams as well as for OUTI targets, in which the dopant is placed in the outer foam instead of the inner foam, for 50- and 70-mg/cm³ foams.

The OUTI Campaign also optimized radiography for this target design relative to the prior campaigns. We moved to a 200-ps pfm from a 500-ps pfm and reduced our down-sampling rate from an 18 × 18-pixel size to a 9 × 9-pixel size. We also optimized our backlighter illumination for this target type, resulting in radiographs such as that shown in Fig. 19. This radiograph includes both the lowest foam density we have ever shot (33 mg/cm³) as well as the largest-ever difference between inner- and outer-foam densities.

This work was performed under the auspices of the U.S. Department of Energy at Los Alamos National Laboratory under Contract No. 8923318CNA000001.



U2860JR

Figure 19

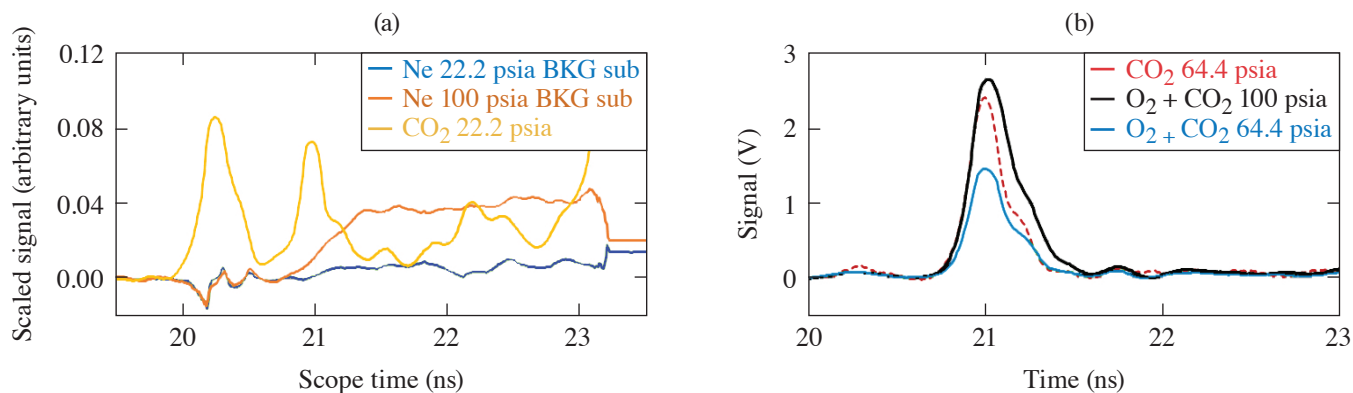
[(a),(b)] Two simulations show the density evolution of an OUTI target with (a) a nominal inner/outer foam density as well as (b) low inner/outer foam density shot 101457. (c) A flat-fielded radiograph (shots 101458 and 101457) shows qualitatively similar behavior to the simulation with low target-foam density in which the shock in the lower-density outer foam runs ahead of the higher-density inner foam. The as-shot foams were 33-mg/cm³ outer and 51-mg/cm³ inner.

GCD Diagdev-21A Investigating Gas Fluorescence in Gas Cherenkov Detectors

Principal Investigators: H. Geppert-Kleinrath, Y. Kim, and K. D. Meaney (LANL); and A. Leatherland (AWE)

The LANL-driven development of the new pulse dilation photomultiplier tube fielded on the gas Cherenkov detector (GCD)⁷ on the NIF allows for unprecedented temporal resolution in gamma reaction history (GRH) measurements of 10 ps (Ref. 8). First measurements of the DT fusion GRH revealed a tail feature not seen before.⁹ Further investigation made clear that gas fluorescence is the cause of the tail seen on GRH. To better understand and be able to mitigate the tail issue, different gases were tested on GCD-1 and GCD-3 on OMEGA (Fig. 20). The gases tested were CO₂ for benchmarking against N₂, Ne, and a mixture of 20% O and 80% CO₂. The targets shot were 1100- μ m-diam Hoppe glass spheres with 4.1- μ m-thick shells, filled to 10 atm of 50/50 DT. The targets were driven with a 60-beam 1-ns square laser drive. The shot day was successful in indicating that both neon gas fill and oxygen are viable paths forward in mitigating the tail issue (see Fig. 20). The neon tail can be subtracted from shot data resulting in cleaner D–T fusion reaction history measurements but reduced signal-to-noise ratio. Oxygen produces less tail than the CO₂ gas currently used in GCD's, but gas cells will need upgrades to accommodate oxygen. Neon was subsequently used to measure the burn width of record-setting shots on the NIF (N210808).

This material is based upon work supported by the Department of Energy National Nuclear Security Administration, Los Alamos National Laboratory Campaign 10 (J. Kline, C-10 Program Manager).



U2861JR

Figure 20

Example data for (a) neon gas fill and (b) an oxygen 20% and CO₂ 80% mixture. The neon tail can be subtracted from shot data for a cleaner signal. Oxygen produces less tail than CO₂ currently used in GCD's.

Thin Separated Fusion Reactants to Study Variation of Observed Complex Kinetic Mix

Principal Investigators: K. D. Meaney, Y. Kim, H. Geppert-Kleinrath, N. Hoffman (LANL); and J. W. Morton and C. R. D. Brown (AWE)

LANL investigates complex, dynamic mix experiments in high-energy-density conditions at the Omega Laser Facility. Los Alamos leverages its gamma-ray diagnostic expertise to make novel, constraining mix experiments. Specifically, the separated reactant technique places deuterium in part of the carbon shell of ICF capsules with hydrogen–tritium in the fuel. The amount of deuterium–tritium fusion is a measure of the amount of mix from that location of the shell into the fuel, with gamma-ray diagnostics allowing potential measurement of the fuel's hydrogen–tritium fusion (releasing 20-MeV gamma ray) as well as the relative timing between the two.

In 2017, a campaign of ultrathin (~150-nm) placed deuterated layers was started to obtain a data set of superhigh spatial resolution shell mix to challenge hydrodynamic codes and quantify kinetic effects. Although the campaign was successful by observing a kinetic, diffusion-dominated mix mechanism in capsule conditions that were previously understood with a turbulent mix layer,¹⁰

the data set also showed a complex, unexpected trend—the amount of mix decreased from the shell that was farther away from the fuel (as expected); however, at around $0.6\text{-}\mu\text{m}$ recession depth, the amount of mix increased again, implying that material in the shell far away from the fuel was mixing in more than the shell that was closer. This unintuitive data, termed the “mix dip,” was investigated in 2019. Testing hypothesized that the fill tube or P1 asymmetries were jetting material from a specific farther location; however, the 2019 data showed that these effects did not cause the mix dip. During this time, simulation and theoretical work continued with calculations showing no clear explanation for the data.

In 2021, we continued to investigate the mix dip, this time doing a direct repeat of the 2017 data of interest with higher spatial resolution and better capsule characterization. The data showed a large amount of variation at the same conditions with no clear observation of the mix dip, suggesting that in 2017, slight variation in the exact placement of the deuterated layer and its thickness could have been responsible for the confusing observed trend. The collected data will be used as part of sensitivity and uncertainty quantification from simulation for historic and future data sets. Likewise, the collected data contributes to a larger body of work of thin separated reactants that have the power to differentiate kinetic mix effects.

This material is based upon work supported by the Department of Energy National Nuclear Security Administration, Los Alamos National Laboratory Campaign 10 (J. Kline, C-10 Program Manager).

Development of the MixIT Diagnostic

Principal Investigators: V. Geppert-Kleinrath, C. Danly, C. Wilde, N. Birge, B. M. Haines, J. Jorgenson, E. Mendoza, L. Tafoya, and P. Volegov (LANL); and S. T. Ivancic, A. Sorce, and T. Burgett (LLE)

A mix of ablator, fill tube, or other high-Z contaminants into the fuel assembly of an ICF implosion is a known performance-limiting process. One of the leading uncertainties in contaminant mass estimates stems from the uncertainty in contaminant mass temperature, which is assumed to be in thermal equilibrium with the fuel. It has recently been shown that portions of contaminant mass do not necessarily thermally equilibrate with the neighboring fuel.¹¹ Therefore, a direct, spatially resolved temperature measurement of the hot spot could provide key contaminant mass temperature constraints crucial to accurate contaminant mass estimates. By combining the principles of a neutron time-of-flight (nTOF) diagnostic and a neutron-imaging system, the MixIT diagnostic is the first of its kind: a temperature imager for ICF.

A sketch of the core components of the MixIT diagnostic is shown in Fig. 21. The tungsten coded aperture projects an image of the neutron source (ICF plasma) onto a 1-D stack of scintillator tiles (EJ 262). One-millimeter optical fibers carry the light from each scintillator tile to the input of the streak camera. In collaboration with the OMEGA Diagnostics Group, OMEGA’s

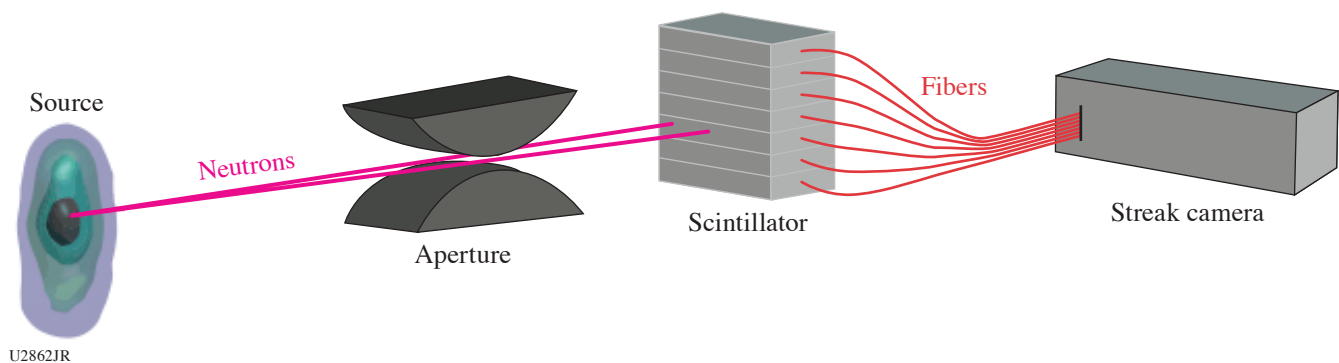


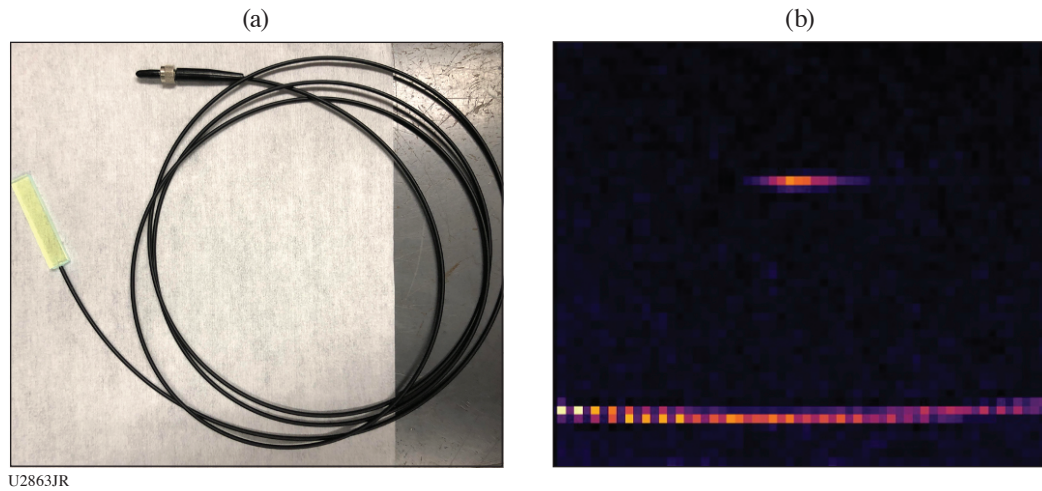
Figure 21

The fundamental components of the MixIT diagnostic. The aperture casts a neutron image of the source onto the 1-D scintillator array, fiber coupled to a streak camera. The recorded image essentially results in a nTOF (or energy) spectrum for each scintillator tile. From the spectra, temperatures can be determined and mapped back to the source.

“System 68” streak camera was fielded for this campaign. The streak camera records the fiber input over a 20-ns window with a resolution of roughly 40 ps. Therefore, a neutron energy spectrum and the plasma temperature are measured by each scintillator tile. This distribution can then be mapped back to the ICF plasma with sufficient knowledge of the aperture point spread function.

The team first captured data on 13 May 2021 during a ride-along on the EnergeticNeutron-21A shot day. A single scintillator pixel was coupled to System 68 to verify the light production and collection indicated by simulation. The shot day was highly successful. The team achieved the primary goal in capturing a streak image for the pixel, thereby validating our simulation efforts. Additionally, the team captured dark-field and charge-coupled device noise data, which have been incorporated into the MixIT diagnostic noise model. The scintillator pixel, along with the corresponding streak data, can be seen in Fig. 22.

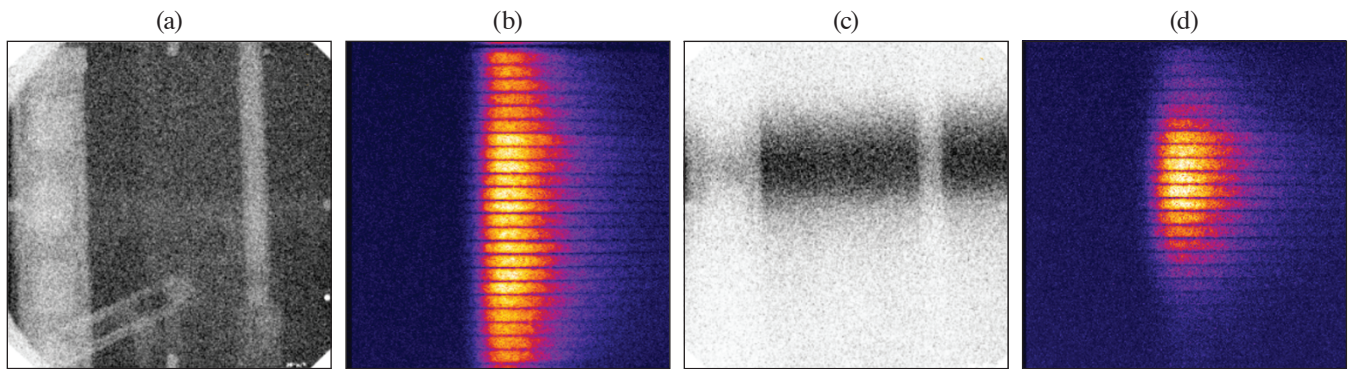
The dedicated shot day, MixIT-21A, took place 9 September 2021. The team accomplished the goal of recording the first-ever spatially resolved temperature data [see Fig. 23(d)]. Calibration, flat-field [Figs. 23(a) and 23(b)], and dark-field data were also recorded. Analysis of the data is ongoing, and preliminary results are anticipated this year.



U2863JR

Figure 22

(a) The scintillator tile fielded during the EnergeticNeutron-21A ride-along. (b) The signal captured by the streak camera. The bottom dotted line corresponds to a frequency comb used to calibrate the time domain of the recorded image. The streak in the middle of the image corresponds to the light from the single pixel.



U2864JR

Figure 23

(a) Image plate and (b) streak camera data captured for calibration shot 101818 without the neutron aperture inserted. (c) Image plate and (d) streak camera data for a production data shot.

1. B. M. Haines *et al.*, *Phys. Plasmas* **20**, 022309 (2013).
2. B. Scheiner *et al.*, *Phys. Plasmas* **27**, 122702 (2020).
3. L. A. Goodwin *et al.*, *Fusion Sci. Technol.* **78**, 66 (2022).
4. F. J. Marshall *et al.*, *Rev. Sci. Instrum.* **92**, 033701 (2021).
5. H. M. Johns *et al.*, *High Energy Density Phys.* **39** (2021).
6. H. M. Johns *et al.*, *LLE 2020 Annual Report*, 338–343, University of Rochester, DOE/NA/3856-1601 (2020).
7. H. W. Herrmann *et al.*, *Rev. Sci. Instrum.* **85**, 11E124 (2014).
8. V. Geppert-Kleinrath *et al.*, *Rev. Sci. Instrum.* **89**, 10I142 (2018).
9. H. Geppert-Kleinrath *et al.*, *High Energy Density Phys.* **37**, 100862 (2020).
10. A. B. Zylstra *et al.*, *Phys. Rev. E* **97**, 061201(R) (2018).
11. B. M. Haines *et al.*, *Nat. Commun.* **11**, 544 (2020).